Secondary electron yield reduction by femtosecond pulse laser-induced periodic surface structuring

J.J.J. Nivas [a,b,c], M. Valadan [b], M. Salvatore [b], R. Fittipaldi [e], M. Himmerlich [d], M. Rimoldi [d], A. Passarelli [a], E. Allahyari [a,b], S.L. Oscurato [b], A. Vecchione [e], C. Altucci [a,b,f], S. Amoruso [a,b,c], A. Andreone [a,b,c], S. Calatroni [d], M.R. Masullo [a,*]

[a] *Istituto Nazionale di Fisica Nucleare, Sezione di Napoli, Complesso Universitario di Monte S. Angelo, Via Cintia, I-80126 Napoli, Italy*
[b] *Dipartimento di Fisica "Ettore Pancini", Università degli Studi di Napoli Federico II, Complesso Universitario di Monte S. Angelo, Via Cintia, I-80126 Napoli, Italy*
[c] *CNR-SPIN, UOS Napoli, Complesso Universitario di Monte S. Angelo, Via Cintia, I-80126 Napoli, Italy*
[d] *CERN, European Organization for Nuclear Research, 1211, Geneva 23, Switzerland*
[e] *CNR-SPIN, UOS Salerno, Via Giovanni Paolo II 132, I-84084 Fisciano, Italy*
[f] *Dipartimento di Scienze Biomediche Avanzate, Università degli Studi di Napoli Federico II, via Pansini 5, I-80131 Napoli, Italy*

ARTICLE INFO

ABSTRACT

The electron-cloud phenomenon is one cause of beam instabilities in high intensity positive particle accelerators. Among the proposed techniques to mitigate or control this detrimental effect, micro-/nano-geometrical modifications of vacuum chamber surfaces are promising to reduce the number of emitted secondary electrons. Femtosecond laser surface structuring readily allows the fabrication of Laser Induced Periodic Surface Structures (LIPSS) and is utilized in several fields, but has not yet been tested for secondary electron emission reduction. In this study, such treatment is carried out on copper samples using linearly and circularly polarized femtosecond laser pulses. The influence of the formed surface textures on the secondary electron yield (SEY) is studied. We investigate the morphological properties as well as the chemical composition by means of SEM, AFM, Raman and XPS analyses. Surface modification with linearly polarized light is more effective than using circularly polarized light, leading to a significant SEY reduction. Even though the SEY maximum is only reduced to a value of ~1.7 compared to standard laser-induced surface roughening approaches, the femtosecond-LIPSS process enables to limit material ablation as well as the production of undesired dust, and drastically reduces the number of redeposited nanoparticles at the surface, which are detrimental for applications in particle accelerators. Moreover, conditioning tests reveal that LIPSS processed Cu can reach SEY values below unity at electron irradiation doses above 10^{-3} C/mm^2.

1. Introduction

In high-energy colliders, storage rings and damping rings operating with positively charged particles, photoemission and secondary emission can give rise to an exponential electron multiplication within the beam chamber [1]. This process may lead to the formation of electron-clouds within the beam pipes that are a source of beam instabilities or degradation [2,3] and local detrimental phenomena, such as heat load to cryogenic system via warm-up of beam pipe walls, pressure rise, etc. [4]. The material parameter that defines the quantity of emitted secondary electrons is the secondary electron yield (SEY), δ, which is the ratio between the number (current I_{SE}) of secondary electrons emitted from the material surface and the number (current I_{PE}) of incident primary electrons, i.e. $\delta = I_{SE}/I_{PE}$ [5]. In addition to particle accelerators, SEY is considered a parameter of great relevance for the system performance degradation in many other fields that face related technological challenges, such as spacecrafts, telecommunication satellites, microwave devices and Hall thrusters [6–8].

The surface topography and electronic properties of a material are the defining factors regarding the number of emitted secondary electrons as well as their ability to escape the surface [9,10]. If the surface of the material is textured or otherwise non-flat, the emitted secondary electrons may end up impinging upon a surface protrusion. Due to their low energy, the emitted secondaries have typically a SEY value much

---

* Corresponding author.
  E-mail address: masullo@na.infn.it (M.R. Masullo).

lower than unity, thus electron scattering on the surface protrusions can generally result in a reduction of the total SEY compared to that of a flat surface [11].

Possible approaches to reduce the SEY by surface modification are based e.g. on functional coatings [12,13], groove-formation and microstructuring at the surface [11,14], nanowire growth [15,16], and generation of microporous structures [17,18]. In addition, engineering of surface morphological features by laser irradiation has been recently considered. Laser sources having nanosecond and picosecond pulse durations have been used to develop ordered grooves or textures (LESS, Laser Engineered Surface Structures) on the material surface, whereas the use of femtosecond (fs) laser pulses is still scarcely investigated [19–23]. Irradiation of solid targets with fs pulses allows fabrication of Laser-Induced Periodic Surface Structures (LIPSS) for a large variety of materials, thus enabling a growing number of technical applications [24–27].

Concerning the target material, copper is largely used for investigation of SEY after laser treatments and it is relevant for application in high-energy particle accelerators such as the Large Hadron Collider (LHC) at CERN [28]. In earlier literature, it has been reported that longer laser pulses generate different textures with characteristic scales larger than the laser wavelength [20]. These surfaces are often decorated by redeposited debris produced during the laser-induced ablation of material, thus leading to nanoroughness of the sample surface [19]. In case of particle accelerators, the release of such debris might result in excessive interactions with the beam and generation of high radiation dose. This could cause premature beam dumps, and occasionally even magnet quench [29,30].

In this paper we investigate how structural modifications induced by fs laser pulses with a characteristic feature size below the laser light wavelength, i.e. in the sub-micrometer range, can influence the SEY of a copper surface. This approach can be optimized to allow formation of structured surfaces with a low particle density, less critical for applications in the vacuum system of particle accelerators. In order to address the role of the surface morphological features on the SEY response, two different kinds of surface textures were considered by exploiting the influence of the laser beam polarization on the generated LIPSS [25,27, 31,32]. Surface textures with well ordered, regular ripples with a subwavelength period were elaborated by using linerly polarized laser light, whereas more disordered surface patterns were obtained utilizing circularly polarized laser light.

As the SEY of a material depends also on its surface chemical composition, we studied the influence of possible adsorbates atoms and surface oxidation, the surface conditioning obtained via electron irradiation, as well as changes induced by sample storage conditions.

2. Sample preparation and experimental analysis

The Cu samples were processed in air using a chirped pulse amplification Yb:KGW laser source providing pulses at a central wavelength of 1030 nm with a pulse duration of $\approx$180 fs and a maximum repetition rate of 200 kHz. The laser source was a custom system similar to Pharos model PH1-SP-1.5 mJ (*Light Conversion*) equipped with a pulse selector that allows defining a sequence of N laser pulses with any value of the repetition rate up to that of the Regenerative Amplifier (RA). In this experiment the laser was operated at a repetition rate of f_p=5 kHz. The target was mounted on a computer controlled XY-translation stage (PP-20, *Micronix USA*) working synchronously with the laser. The target was a 1 mm thick oxygen free copper (Cu-OFE, UNS C10100) square plate with dimensions of $\approx$10$\times$10 mm^2. Half of the samples (hereafter denoted as OFC) were used as received after passing a degreasing process with detergents and DI water rinsing only, while the other half was in addition passivated by a chromic acid treatment as per CERN cleaning protocols [33] (POFC samples). The period between chemical cleaning

and laser treatment was several weeks, in which the OFC samples underwent oxidation. During the experiment, the laser light was focused in air onto the target material at normal incidence by a plano-convex lens with focal length of 200 mm. The spot radius of the Gaussian laser beam on the target surface was obtained by analyzing the variation of the area modified by laser irradiation vs laser energy following the methods proposed by Liu [34–36] and also supported by theoretical findings for the case of fs laser ablation [37]. The laser beam radius is $w_0 \approx 40$ μm and the corresponding peak fluence for the Gaussian beam is calculated using $F_p = (2E)/(\pi w_0^2)$ with E being the pulse energy. Femtosecond laser irradiation of a metallic sample typically leads to the formation of LIPSS in form of ripples, with subwavelength period and decorated by nanometer sized features [25,27]. It is worth noticing that ripple features may also critically depend on the properties of the target and laser parameters [26,38,39]. In the case of copper irradiated at normal incidence, after tens of pulses well-defined subwavelength structures are typically generated, whose orientation depends on the incident light polarization. In the current experiment, the main goal was to form surface structures across a millimeter size area, achieved by raster-scanning of the laser beam on the surface, i.e. by moving the target at a velocity v_s. Hence, the number of overlapped pulses N_O for defined laser parameters is determined by v_s [40]. We selected two scanning velocity settings ($v_s = 1$ mm/s and 2 mm/s) that lead to a number of overlapped pulses of $N_O \approx 400$ and $N_O \approx 200$, respectively (N_O $= (2w_0 f_p)/v_s$). In both cases, the pulse overlap $\left(1 - \frac{1}{N_O}\right)$ is greater than 99%. Laser surface structuring of the samples was carried out across an area of 8×8 mm^2 by writing a pattern of parallel lines. This was achieved by a continuous bidirectional raster scan of the laser beam on the sample along the horizontal direction and a hatch distance Δ along the vertical direction. However, it is worth noticing that even if we used a laser repetition rate of 5 kHz and scanning speed of the order of 1–2 mm/s, texturing of larger areas by laser irradiation is nowadays possible by an appropriate experimental setup [41–43].

In case of linear polarization, different samples were produced by varying the laser pulseenergy and scanning speed in order to select optimal experimental conditions, as will be illustrated later (see Fig. 1). In particular, the scanning direction was held parallel to the light polarization direction and the line separation was set to $\Delta = 110$ μm.

Previous articles [31,32] have shown that while linear polarization leads to regular periodic ripples, more disordered surface patterns are induced by circularly polarized light. Therefore, the exploitation of another surface texture can allow evidencing possible influence of the surface morphological features on the SEY response, as will be discussed later. In an attempt to identify such behaviors, some samples were also fabricated by irradiating the target surface with circularly polarized light. In this respect, it is worth noticing that ripple formation with linearly polarized laser light is rationalized by considering the interference between the incoming light and surface scattered waves, as e.g. surface plasmon polaritons [25,27,44,45]. In this case, the progressive generation of a grating-like surface strengthens the formation of a rippled surface pattern by means of feedback mechanisms [25,27,45]. Instead, for circular polarization such an effect is reduced due to the more random spatial distribution of the surface scattered waves launched on the surface. Hence, for circular polarization, some of the experimental parameters were modified in order to obtain a qualitatively similar level of surface texturing, while keeping the same beam spot size.

The experimental analysis of the samples involves several measurements. Morphological features of the irradiated copper surface were analyzed by Field Emission Scanning Electron Microscopy (FE-SEM) (Zeiss Sigma) and Atomic Force Microscopy (AFM) (Witec Alpha 300 RAS) analyzes. SEM images were recorded via secondary electron (SE) detection with a lateral resolution of 1.3 nm at 10 kV. Raman

spectroscopy (Witec Alpha 300 RAS) was also utilised to investigate any possible variation between the laser irradiated and the pristine target surface.

Samples were stored in plastic sample boxes after laser processing and shipped to CERN for further analysis. The surface chemical composition was characterized by X-ray Photoelectron Spectroscopy using a commercial ultra-high vacuum (UHV) system (SPECS Surface Nano Analysis GmbH, Berlin, Germany) with a base pressure of $< 2 \times 10^{-10}$ mbar that is equipped with a hemispherical electron energy analyzer with 9 channeltrons (Phoibos 150) and a monochromatic AlKα X-ray source (XR50M, $h\nu = 1486.7$ eV). The depth of information for these analyzes is 5 - 8 nm. For measurements of the secondary electron yield between 50 and 1800 eV primary electron energy, an electron beam of ~2 nA as generated by a Kimball Physics ELG-2 electron gun at a distance of 2 cm to the sample, was focused to a spot diameter of 1 mm on the surface. The details of the measurement and the implemented experimental conditions are described in reference [46]. A sample bias of ± 47.1 V was used and SEY curves were measured in all cases at three different sample positions. The average values are given with a statistical measurement uncertainty that amounts to below 0.05 for a confidence level of 68.3%, if not otherwise indicated. Selected sample surfaces were re-characterized by SEY and XPS measurements after 9 months of sample storage in the sample boxes. Tests on the effect of electron-irradiation (conditioning) on the SEY were at this stage performed in a second UHV system equipped with a home-built setup for SEY analysis including a positively biased (+ 40 V) collector that surrounds the negatively biased sample (−15 V), which is exposed to an electron beam of ~2 nA generated by an ELG-2 electron gun. To study electron-induced conditioning, a second source (flood gun FG15/40, SPECS) was operated, and the dose of 250 eV electrons impinging on the surface was calibrated using Faraday cup measurements.

3. Results and discussion

In order to identify the best experimental configuration for SEY reduction on copper using LIPSS generation, the effect of laser pulse energy and scanning speed on the LIPSS features was investigated by carrying out structuring experiments with the linearly polarized beam on OFC samples. Selected SEM images of the sample surface, as shown in Fig. 1, display the formation of sub-wavelength periodic surface features, termed as surface ripples or low spatial frequency LIPSS (LSFL). A series of samples were prepared by using two different scanning speeds v_s *(1 mm/s, 2 mm/s)* and three different laser pulse energies *E*, namely *40 μJ, 60 μJ and 100 μJ*. The corresponding values of the laser peak fluence F_p are 1.6, 2.4 and 4.0 J/cm^2.
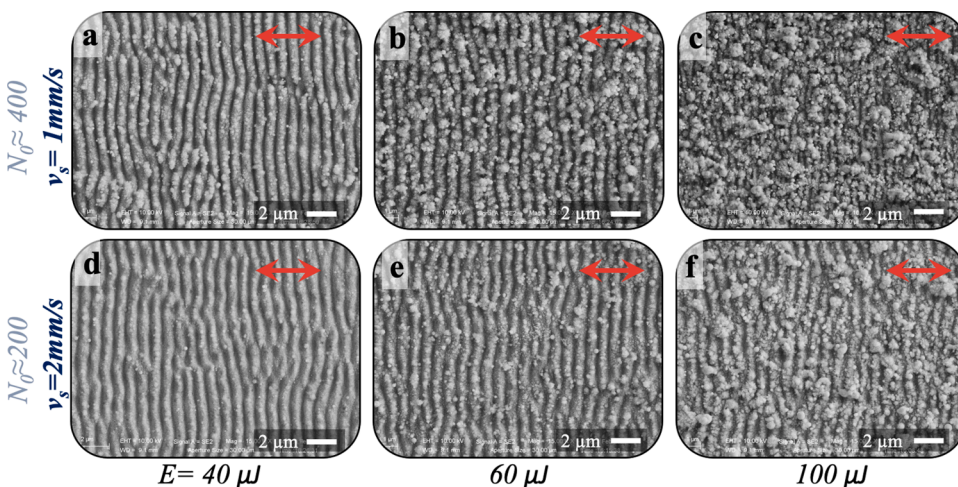
These surface ripples present a preferential orientation perpendicular to the laser polarization, orientation related to the LIPSS formation mechanism that is explained by an interference phenomenon as reported before [25,27,40,47,48]. This effect, in turn, induces a spatial modulation of the light intensity that is eventually engraved onto the material surface. A spatial periodicity of *Λ≈800* nm is observed, as typically found on metal targets [25–27]. At higher pulse energy, the surface is also decorated by sparse nanoparticles that have been back-deposited onto the sample as a consequence of the air confinement [25,27,49, 50]. Ripples formed at the pulse energy *E = 40 μJ* (F_p=1.6 J/cm^2) are comparatively cleaner with less abundance of nanoparticles and are more clearly visible. Moreover, variation of the scanning speed, defining the number of overlapped pulses, further affects the amount of material ablated from the surface and the final texture. Thus, at lower scanning speed a deeper valley between subwavelength ripples is observed, as clearly visualized from the comparison between lower and upper panels of Fig. 1. The number of overlapped pulses also influences the spatial period in either of these cases, i.e. an increase of N_0 typically results in a reduction of the spatial ripple period until a plateau regime is reached at very large pulse number [47,51]. The ripple periods evaluated from panels (a) and (d) of Fig. 1 for *E = 40 μJ* (F_p=1.6 J/cm^2) are (820±25) nm and (860±30) nm, respectively. For the same figures, analysis of AFM data using the software *Gwyddion 2.50*, revealed a root-mean-square (RMS) roughness of 290 nm and 185 nm respectively, and a peak-to-valley distance of the ripples of (370 ± 60) nm and (220 ± 40) nm for $N_0 = 400$ and N_0= 200 pulses, respectively. Besides ripples, the sample surface presents a larger scale surface modulation in the range of several tens of micrometers induced by the raster scanning procedure (an example of this wavy nature of the surface is shown in Fig. 4(f)). The periodicity of this modulation closely matches the line separation used in the laser scanning process and likely results from the spatial variation of the fluence associated to the Gaussian profile of the laser beam along the direction perpendicular to the scan direction. In fact, the variable spatial fluence profile typically leads to the imprinting of a very shallow trench for each scanning line with a depth of few microns (as shown, for example, in Fig. 4(f)). In our experimental conditions, the rather similar values of laser beam diameter, $2w_0$, and of line separation, Δ, eventually result in the observed wavy modulation instead of a surface structure with well separated and deep micro-trenches as typically observed if $\Delta \geq 4w_0$ [20,21,52]. Therefore, the laser surface structuring process allows fabricating samples with a triple-scale hierarchical surface structure formed by a pattern of very shallow parallel large micro-trenches, a finer texture of ripples with sub-micrometer period and a random decoration of nanoparticles.

Furthermore, in order to study the influence of the surface

Fig. 1. SEM images of OFC copper surfaces after structuring at varying pulse energy *E* and beam scanning speed v_s. For panel (a) to (c) v_s= 1 mm/s ($N_0 \approx 400$) and for panel (d) to (f) v_s= 2 mm/s ($N_0 \approx 200$). For each condition, the value of the pulse energy *E* is reported at the bottom of the corresponding panels and the corresponding values of the laser peak fluence F_p are 1.6, 2.4 and 4.0 J/cm^2. The direction of the linear polarization is indicated by the red arrows. The laser repetition rate is f_p= 5 kHz.

morphological features on the SEY response, same samples have been produced using circularly polarized laser beams. In this case the ripples are arranged in a rather random manner due to the propagation of surface waves supported in all directions. However, the processing parameters, as scanning speed, laser energy and line separation, were selected in order to get samples surfaces showing rather similar surface characteristics at small scale.

OFC and POFC samples were laser textured with linear polarization (OFC-lin and POFC-lin) at a pulse energy of 40 μJ (F_p=1.6 J/cm^2) and a scanning velocity of v_s= 2 mm/s. Samples with a similar level of surface structuring were also produced with circularly (OFC-circ and POFC-circ) polarized beams at a laser energy of 30 μJ (F_p=1.2 J/cm^2), a scanning velocity v_s= 1 mm/s, and a line separation of Δ =75 μm. Fig. 2 reports a comparative analysis of the LIPSS generated on OFC and POFC samples using these experimental conditions.

The surface features of the samples in Fig. 2 are primarily different because of the large dependence of LIPSS on the incident polarization. In case of linear polarization, the ripples always show a preferential alignment in a direction normal to the polarization, with some characteristic bending and bifurcation phenomena. However, due to a proper selection of the processing parameters the samples show rather similar surface characteristics at small scale, as evidenced in the Fig. 2.

The contrast differences in the SEM images of Fig. 2(a) and (c) could be an indication that the morphology of the ripples for the two copper samples, OFC and POFC, exhibit differences, i.e. that in the case of OFC, deeper and clearly defined LIPSS features are formed. On the other side, the ripple periods evaluated from panels (a) and (c) for OFC-lin and POFC-lin are of the same order (~800 nm).

To provide a clearer idea of the effects of laser treatment on the passivated copper, Fig. 3 shows SEM images of the POFC samples irradiated with linearly and circularly polarized beams. Micrographs captured at lower magnification in panels (a) and (b) display the trenches produced by laser scanning. Due to the Gaussian spatial distribution of the laser intensity and the partial overlap between the lines, the surface morphology presents some variations across the sample, from the center towards the edge of the trenches. Panels (c) and (d) report SEM micrographs registered at higher magnification together with zoomed views, in the lower and upper insets, of the surface features formed in the more and less intense parts of the beam, respectively. As a result of the spatial distribution of the laser intensity, there is a small area between each line, where the beam intensity is at its minimum value. For linear polarization (panel (c)), this region is covered with periodic features slightly different from those of the more intense part

where ablative ripples are clearly formed. In the case of circular polarization (panel (d)), the region irradiated by the less intense part of the beam is covered with well-arranged nano-bumps, whose shape reminds droplets from a molten metal and likely formed by melting and re-solidification of deposited nanoparticles. This assumption is also supported by the observation that in this case there exists only a negligible decoration of the surface by nanoparticles. In the area exposed to a lower intensity, for the linear polarization the LIPSS appear to be formed by arrangement of nanoparticles or debris redeposited onto the surface. However, in this case the arrangement of the nanoparticle-assembled features depends on the direction of the linear polarization of the incident laser beam, similarly to the behavior of the standard ablative ripples. The formation of self-organized ripples through a progressive aggregation of nanoparticles has been observed both with continuous and pulsed laser irradiation [53,54]. In particular, Talbi et al. have shown that, for irradiation with ultrashort laser pulses at low irradiance (at fluences below the ablation threshold), an initially random distribution of nanoparticles can be transformed into subwavelength scale, well-ordered arrangement of nanoparticle-based LIPSS oriented perpendicularly to the polarization direction [54].

Panels (e) and (f) of Fig. 3 report the spectra obtained by two-dimensional fast Fourier transformations (2D-FFT) of the SEM images measured in the sample region of intense laser illumination for both polarizations. The sickle-shaped 2D-FFT map shown in panel (e) corresponds to periodic parallel ripples with inherent bending and bifurcations, as typically observed in the case of irradiation with a linearly polarized beam [24,45]. Instead, a circular pattern is formed indicating a lack of spatial anisotropy in the case of circular polarization.

The sample surface is further characterized by AFM analyzes (see Fig. 4) to address geometric dimensions of the formed structures for the OFC (a-b) and POFC (c-d) samples. The well-ordered parallel ripples can be clearly seen in the case of linear polarization (panels (a) and (c)), with deeper ripples in the case of the OFC sample and shallower ones for the POFC sample. Topography line profiles extracted from the AFM data of panels (a) and (c) are shown in panel (e), clearly addressing the differences in the profile height between OFC and POFC samples. It is worth mentioning that to obtain a decent AFM profile as those shown in panel (e), the depth profile had to be measured in a sample region irradiated by lower laser intensity where the height of the surface irregularities is comparatively negligible. Considering these profiles, average depths of the ripples d_{avg} (valley-to-peak) are evaluated to be (210 ± 15) nm in the case of OFC-lin and (105 ± 10) nm for POFC-lin. For completeness, the d_{avg} evaluated where the beam intensity is maximum is (270 ± 40) nm in
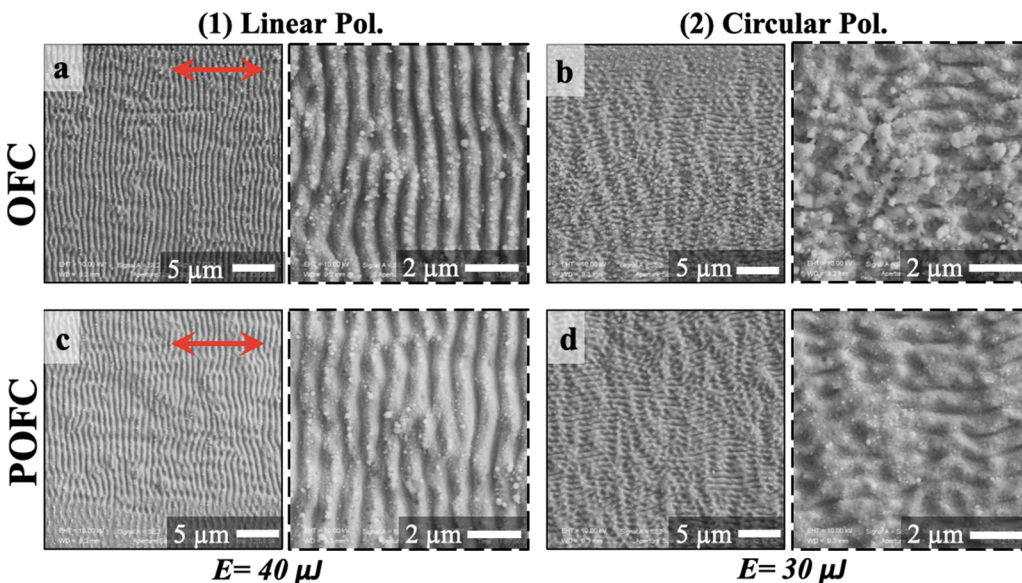

Fig. 2. SEM images of the OFC and POFC copper sample surface after structuring with linearly (a, c) and circularly (b, d) polarized fs laser pulses, respectively. Higher magnification views of the subwavelength features are shown in the dashed boxes on the right side of each panel. For panels (a) and (c), the direction of the linear polarization is indicated by the red arrows. The used pulse energy is E = 40 μJ (F_p=1.6 J/cm^2), v_s= 2 mm/s for the linear and E = 30 μJ (F_p=1.2 J/cm^2),v_s= 1 mm/s for the circular polarization, respectively.
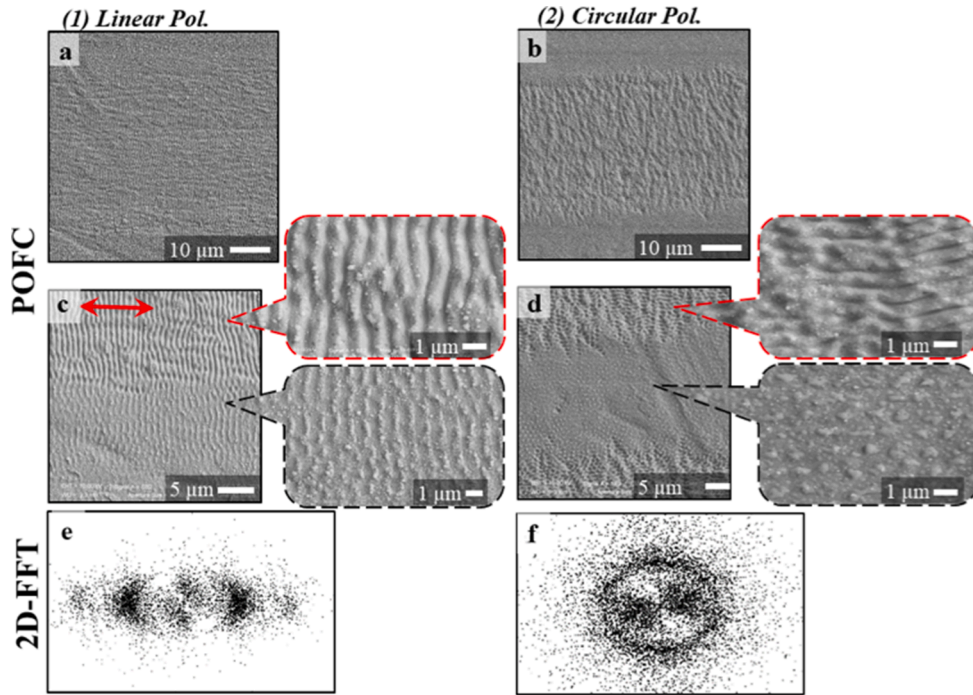
Fig. 3. SEM images of the POFC copper sample surface structure generated by fs pulses with linear ($E \approx 40\mu J$, $v_s = 2$ mm/s, $N_0 \approx 200$) and circular ($E \approx 30\mu J$, $v_s = 1$ mm/s, $N_0 \approx 400$) polarizations. For both polarizations, the higher magnification micrographs in the upper and lower insets of panels (c) and (d) show subwavelength features formed in the more and less intense parts of the beam, respectively. Panels (e) and (f) display 2D-FFT obtained from the SEM images of the surface corresponding to the intense part of the beam. The red arrow indicates the light polarization direction.
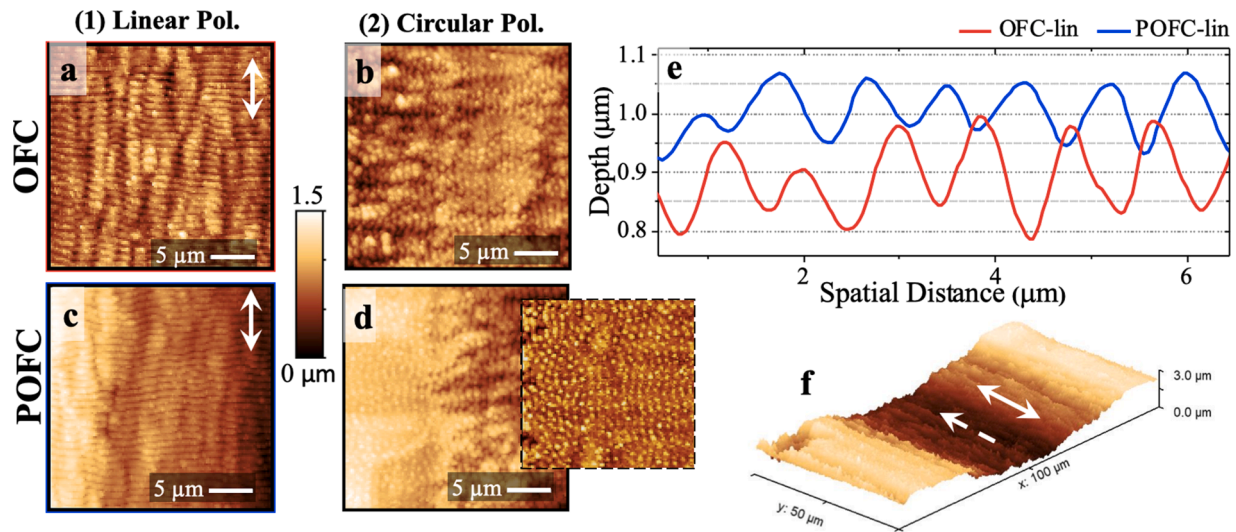

Fig. 4. AFM images of structured Cu surfaces. Panels (a-d) show scans of samples OFC-lin, OFC-circ, POFC-lin and POFC-circ, respectively. The laser processing parameters are $E \approx 40\mu J$, $v_s = 2$ mm/s, $N_0 \approx 200$ for the linear polarization and $E \approx 30\mu J$, $v_s = 1$ mm/s, $N_0 \approx 400$ for the circular polarization, respectively. A magnified view of panel (d) is given in the inset. Panel (e) shows topography line profiles obtained from the AFM scans displayed in panels (a and c). In panel (f), an AFM image at lower resolution shows the wavy profile of the surface, the periods between valleys and peaks are in the order of several tens of microns (110 μm for linear and 75 μm for circular polarization). In the AFM images the direction of the linear polarization is indicated in panels (a, c and f) by solid white arrows, whereas the dashed arrow in panel (f) indicates the scanning direction.

the case of OFC-lin and (230 ± 40) nm for POFC-lin. As already mentioned, in this region the measured depth may not correspond to the real peak-to-valley depth of ripples because of the slope of the underlying surface profile created by the laser beam and due to the presence of some debris in this region.

In agreement with the indications from SEM contrast, there exists a slight dependency of the peak-to-valley height for the structures formed in OFC and POFC samples, which primarily results from the difference in the surface quality of the pristine samples. The surface of the POFC samples is reflective due to the chemical passivation that suppresses subsequent surface oxidation, even though the passivation process

etches the surface leading to slight roughening. In contrast, after degreasing and shipping, the non-passivated OFC samples exhibited a slight color change (darker visual appearance) which is an indication for the formation of a natural oxide/hydroxide protection layer with different optical properties, i.e. higher absorptivity. This in turn leads to certain differences in the laser-light matter interaction for the two cases such as the effective value of the absorbed laser energy, which in the end affects the resulting ripple height. The slight increase in the porosity of the surface induced by the chemical passivation process should promote ripple formation [51,55,56]. However, the ripples observed for the POFC sample are shallower than OFC one. This is likely due to a shiner

surface of the POFC sample that reduces the laser energy absorption as well as to a not so different level of roughness with respect to the commercial OFC samples.

The AFM images in the case of the circularly polarized beam are shown in panels (b) and (d). These images also demonstrate the unordered structure of the surfaces formed in the case of circular polarization. Here the surface appears to be decorated with randomly oriented features in regions irradiated by the intense part of the beam, and arrays of nano-bumps in the region where the beam intensity is lower. A magnified scan of such nano-bumps is displayed as an inset in panel (d) of Fig. 4. In panel (f), an AFM image of a larger area of the sample surface is provided, to address the wavy profile of the surface with valleys and peaks originating from the spatial difference in laser light intensity during raster-scanning with hatch distances Δ being larger than the beam diameter. The period of these variations is equivalent to Δ, i.e. 110 μm for the linear polarization and 75 μm for the circular polarization. For all processed samples, the depth of this undulation is less than 3 μm.

Information on the surface composition of the samples, including possible contaminants, was obtained by Raman spectroscopy and XPS analyzes. The Raman spectra, which refer to a comparison between the pristine and treated surfaces, are identical for the implemented laser light polarizations and the different surface treatments (OFC and POFC). Fig. 5(a) reports a typical example of the Raman spectra recorded on a laser-irradiated Cu sample (circular polarization) and on the pristine region of an OFC sample. Both spectra exhibit the characteristic series of Raman peaks associated to Cu_2O [57,58], clearly visible in the region below 200 cm^{-1}, and weaker peaks associated to imperfection of crystalline structure of copper oxides, between 400 cm^{-1} and 600 cm^{-1}, thus suggesting a predominance of Cu_2O oxides on the surface. Interestingly, the two spectra show large similarities thus suggesting a minimal change to the surface composition induced on the laser irradiated area with respect to the untreated one. A likely explanation is that the copper surface is mainly oxidized during exposure to air.

Fig. 5(b) includes Cu 2p, Cu LMM and O 1s XPS core level and Auger spectra recorded for OFC and POFC samples as received after laser treatment and after 9 months of storage in plastic boxes. There are no distinct differences after laser treatment for the two different pre-treatment procedures, i.e. the OFC and POFC samples. It is important to note that for the POFC samples, no Cr signal is detectable by XPS after the laser-treatment, which is typically the case for passivated Cu surfaces. This indicates that the laser-induced surface structuring not only changes the topography but also removes the surface passivation for POFC samples. Consequently, both initial sample surface types (OFC and POFC) exhibit the same surface composition after treatment and are prone to surface reactions in ambient conditions comparable to a degreased flat Cu surface. The spectral features resemble those of an

oxidized Cu_2O surface with a hydroxide top layer [59,60] with two states in the O 1s spectrum at 530.4 eV and 531.5 eV and two features in the Cu 2p$_{3/2}$ line at 932.4 eV and 934.4 eV, while the Cu LMM Auger-excitation at 916.8 eV is rather broadened. For the Cu_2O signal in the Cu 2p$_{3/2}$ state, this would correspond to an Auger parameter of 1849.2 eV. Hydrocarbon surface impurities are also detected and partly contribute to the O 1s emission (C 1s spectra not shown). We have estimated the surface composition by considering the spectral areas of the main core level of each detected element and weighting them with their respective sensitivity factors [61] assuming a homogenous elemental distribution [62], which slightly overestimates the contribution of a species located at the outermost surface, such as adsorbates. Table 1 shows the resulting elemental contributions.

It is worth mentioning that Cu_2O and hydroxide naturally form in air at room temperature and their existence at the surface after the LIPSS treatment in air indicates no strong energy intake to induce non-equilibrium Cu surface oxidation processes. In contrast, if pulsed lasers with higher fluence are used for surface processing of Cu in air, typically passivated particles with CuO surface are generated within the expanding plasma plume of ablated material and partially redeposited onto the surface [21,44]. The fact, that this is not the case for the LIPSS processing and that no CuO is formed, suggests that the typically utilized laser-treatment in inert atmosphere, to avoid strong oxidation [21], would eventually not be necessary. The surface properties of samples treated with linearly polarized light were re-evaluated after 9 months of storage in plastic boxes. The corresponding XPS measurements reveal an increase of the hydroxide content at the surface and a further uptake of hydrocarbon surface impurities as also typically found for initially degreased and afterwards air-exposed Cu surfaces.

Fig. 6 reports the results of SEY measurements on the structured copper samples and Table 2 details the obtained maximum SEY values. Compared to degreased flat Cu with airborne adsorbates (dashed black line) [39], the samples OFC-lin and POFC-lin exhibit a reduced SEY for primary electron energies below approximately 1000 eV, which is the typical energy range of accelerated electrons in case of electron-cloud built-up in the LHC [3].

The SEY curves of OFC-circ and POFC-circ are comparable to that of

Table 1
Surface composition (in at.%) based on the quantitative XPS analysis for Cu surfaces after laser treatment and after further storage.

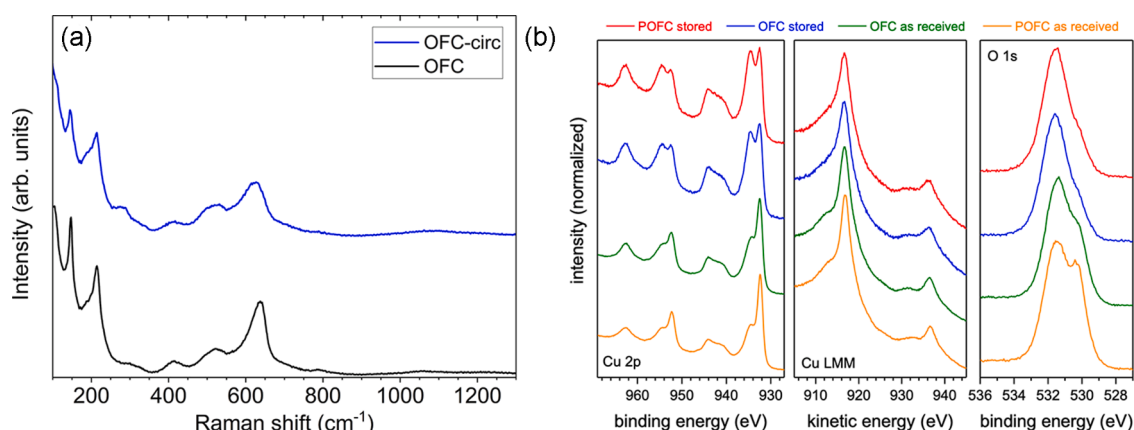| Sample / Element	Cu	O	C
POFC-lin as received	36.8	35.4	27.8
OFC-lin as received	36.3	35.7	28.0
POFC-lin stored	21.5	32.4	46.1
OFC-lin stored	21.2	32.3	46.6

Fig. 5. (a) Typical Raman spectra of untreated and laser-treated OFC copper samples. (b) XPS spectra of the Cu 2p, Cu LMM and O 1s emission of laser-treated Cu surfaces with different surface preparation (OFC and POFC) as received after laser processing and after 9 months of storage in plastic boxes.
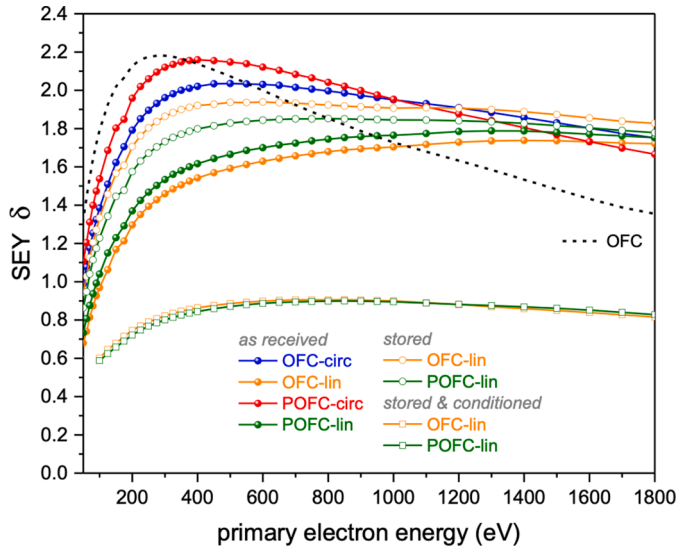
Fig. 6. Primary electron energy dependence of the SEY for OFC and POFC samples processed with linearly and circularly polarized laser light. For samples processed with linearly polarized light, the SEY is also shown after 9 months storage in plastic sample boxes and after subsequent conditioning via electron irradiation in UHV.

Table 2
SEY maximum δ_{max} and its related energy $E(\delta_{max})$ for the different laser-treatment parameters and post-treatment surface conditions.

Sample	δ_{max}	$E(\delta_{max})$
OFC degreased	2.18	300 eV
POFC-lin as received	1.79	1300 eV
OFC-lin as received	1.74	1400 eV
POFC-circ as received	2.16	400 eV
OFC-circ as received	2.03	500 eV
POFC-lin stored	1.85	800 eV
OFC-lin stored	1.94	600 eV
POFC-lin stored & conditioned	0.90	850 eV
OFC-lin stored & conditioned	0.91	850 eV

flat Cu samples, excepted for a shift of the maximum SEY to higher primary energy. According to the analogous surface stoichiometry of the as-received samples (see XPS results), these experimental findings indicate that the differences in SEY mainly originate from morphological differences of the sample surface, i.e. are induced by the different surface topography and ripple pattern inscribed by the fs laser pulses. Utilizing different technologies, earlier studies have shown in general that surface patterning and especially trench and side facet formation is an efficient approach to lower the effective SEY of a material's surface [11,44].

The larger SEY values and lower SEY maximum energy observed in the case of OFC-circ and POFC-circ samples indicate that the spatial arrangement of the submicrometer-sized surface features has a prominent role in the secondary electron emission from the modified copper surface. In fact, the periodic subwavelength ripples with an ordered arrangement formed for linear polarization are more beneficial for SEY reduction in comparison to the randomly oriented structures generated by circularly polarized laser light. The SEY of OFC-lin and POFC-lin samples show a very similar trend as a function of primary electron energy, but OFC-lin exhibits slightly lower values. It is worth noticing that the major difference in the topography of these two samples is the depth of the surface modulations. As identified in the AFM and SEM analyzes, in the case of OFC-lin the ripples are slightly deeper than for POFC-lin, while the average ripple period is very similar. This observation points towards the fact that an increased aspect ratio of the

surface ripples observed for OFC-lin could be beneficial, even though the difference in SEY is < 0.1. The aspect ratio mentioned here is only related to the periodic subwavelength ripples and does not consider the long-range surface waviness induced by the raster scanning, which can also have an effect on the SEY.

We have re-evaluated the SEY of OFC-lin and POFC-lin samples after 9 months of storage. The SEY increased, especially in the energy region between 50 and 1000 eV. In this case, the changes compared to the as-received samples are induced by the chemical modification of the surface (surface impurity uptake), since the topography remained unchanged.

The obtained SEY reduction, compared to a flat Cu surface, is not sufficient to avoid any initial electron-cloud build-up in particle accelerators, which would require ideally $\delta \leq 1$. Nevertheless, the impact of the ordered subwavelength LIPSS induced by fs laser irradiation on the SEY is evident and might provide a further route to elaborate structured metallic surfaces with improved characteristics, by appropriate design of large-scale textures defined by raster scanning and finer-scale features intrinsically formed via fs-pulsed laser surface structuring. Moreover, as the state-of-the-art technology of using flat Cu surfaces in the LHC relies on electron-induced conditioning in initial so-called scrubbing runs, where the electron irradiation due to the electron-cloud itself helps reducing the SEY of OFC to 1.1 - 1.2 [46,63], the LIPSS-induced topography modification could also have impact on the conditioning trends of processed surfaces. We have therefore performed laboratory experiments of electron-induced conditioning by exposing POFC-lin and OFC-lin samples after the storage period to a beam of 250 eV electrons using a flood gun. The SEY curves after full conditioning (dose >10^{-2}C/mm^2) are included in Fig. 6. Fig. 7 shows the variation of their maximum SEY in dependence of the applied electron dose in comparison to a standard degreased flat Cu sample (OFC) [46]. Based on the XPS results discussed above of as received and aged samples, no differences are expected between the flat reference and the LIPSS Cu surfaces in terms of interaction processes and modification of the surface composition induced by the conditioning. Besides the difference in topography, chemically the surfaces are comparable and the slight local variation of electron impact angle for the LIPSS samples is believed to be of minor influence. We therefore anticipate that the same physical and chemical
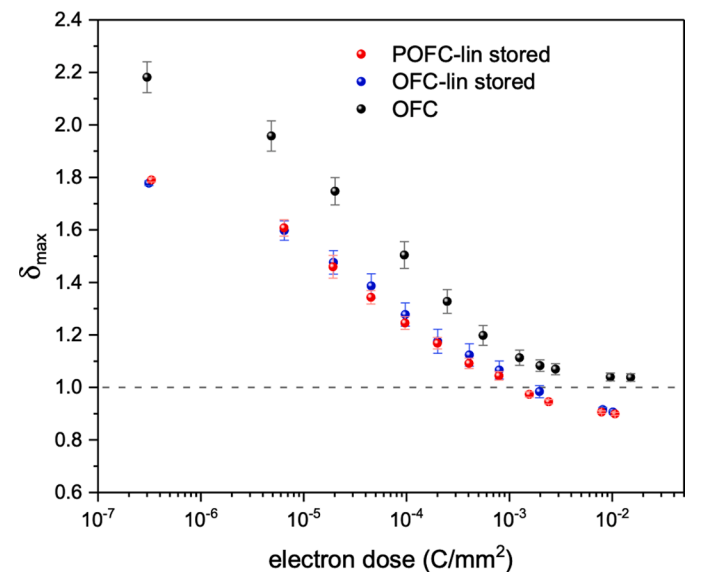

Fig. 7. Variation of the SEY maximum of samples POFC-lin and OFC-lin after storage in comparison to a flat, degreased Cu sample (OFC) [17] upon irradiation with 250 eV electrons in dependence of their dose. The error bars represent the statistical measurement uncertainties for a confidence level of 68.3% based on three measurements performed in different locations of the samples.

processes result during 250 eV electron irradiation, which modify the surface stoichiometry via transformation of existing hydroxides and graphitization of surface hydrocarbons as for flat Cu samples [40]. Consequently, a SEY reduction occurs due to surface stoichiometry transformation. The results clearly show that δ_{max} tends to decrease below unity in the test measurements with an external electron source (Fig. 7), which is not the case for flat copper samples. This is attributed to the difference in surface topography in the same manner as for the as-received samples. The electron dose of $\sim 1 \times 10^{-3} \text{C/mm}^2$ required to obtain $\delta_{max} \leq 1$ has to be compared with the maximum surface dose of $\sim 5 \times 10^{-3} \text{C/mm}^2$ accumulated during the extensive 10 days scrubbing procedure at the beginning of LHC Run 2 [64]. In addition, the threshold of $\delta_{max} \leq 1$ was reached for a dose 5 times lower than what required for reaching the final SEY value during conditioning of flat Cu, which is promising to reduce scrubbing efforts and time in particle accelerator operation. LIPSS on Cu could then be a sufficient solution to reduce the SEY close to unity in a scrubbing run, and thus to mitigate electron-cloud formation.

4. Conclusions

Irradiation of solid targets with femto-second pulses is performed for producing LIPSS on copper samples for SEY reduction. The effects of laser processing parameters on the surface structured textures, as ripples and surface modulation, were investigated to optimize the formation of structured surfaces bearing a low particle density, an essential requirement for applications in the vacuum system of particle accelerators. Based on SEM analyzes of the obtained surface structures after a preliminary irradiation using varying scanning speeds and laser pulse energy, it was decided to further evaluate processing with an energy of 40 μJ and 30 μJ for linearly and circularly polarized laser light, respectively. Test samples were processed starting from passivated (POFC) and degreased (OFC) copper pieces. The fs laser surface structuring allows fabrication of samples with a triple-scale hierarchical surface structure formed by a pattern of very shallow (depth < 3 μm) parallel micro-trenches, a finer texture of ripples or dots with sub-micron period and a random decoration of nanoparticles. Raman spectroscopy and XPS analysis show that the sample surface maintains the same chemical composition after the treatment.

The comparison between illumination by linearly or circularly polarized light shows that the orientation of the formed sub-wavelength periodic surface features affects the SEY values. In particular, a parallel oriented grating structure produced by linear light polarization can better supress the secondary electron emission with respect to randomly oriented arrangements created using circular polarization. Moreover, the ablated crater morphology depends on the preparation of the Cu samples prior to laser processing. In the case of passivated samples, their higher optical reflectivity reduces the ablation of the surface compared to degreased but oxidized samples for the same laser conditions.

The modification of the surface topography is a very efficient and promising method to reduce the SEY. Nevertheless, it is important to study the behavior of these structures when exposed to real machine environments and their influence on vacuum performance. From the measurements reported in this article using fs LIPSS, it seems that the small ablation depth and the ripple height in the range of a few hundred nanometers generates a surface with higher SEY values compared to the classical LESS process. At the same time, the absence of redeposited oxidized particles and the obtained micro-trench depth of below 3 μm are less prone to induce any impedance problems for beam induced image currents or to cause premature beam dumps due to excessive interactions with released particles. The low pulse energy ($E = 40 \, \mu J$ and $30 \, \mu J$) used in our fs LIPSS processing, together with the scanning speed, affects the amount of material ablated from the surface and the final texture: the ripples are comparatively cleaner, with less abundance of nanoparticles compared to laser processing at higher pulse energy. Furthermore, measurements have shown that, during the LIPSS processing, no CuO is formed and no particles with passivated CuO surface are generated, suggesting that it would not be necessary to work in inert atmosphere to avoid strong oxidation.

Finally, conditioning tests performed on stored samples demonstrated that the SEY of LIPSS Cu surface reduces to below unity for an electron dose of $\sim 1 \times 10^{-3} \text{C/mm}^2$. The conditioning may improve when achieving a higher aspect ratio of the undulating surface via LIPSS. Ideally, the initial SEY maximum should be as low as 1.4 - 1.5 and the dose for mild conditioning should be $< 5 \times 10^{-4} \text{C/mm}^2$. These findings are in line with ongoing developments to make the laser treatment of beam-facing accelerator components a method that could allow surface processing for safe accelerator operation, i.e. to avoid particulate-related risks or surface impedance problems. The obtained SEY and conditioning performance illustrates a new pathway for surface engineering of vacuum components by LIPSS, which is expected to have the potential for further optimization of the surface topography by adapted laser processing conditions.

Author contributions

Carlo Altucci, Salvatore Amoruso, Antonello Andreone, Sergio Calatroni and Maria Rosaria Masullo: conceived the aim of the research. Jijil JJ Nivas and Mohammadhassan Valadan: carried out the Laser Surface Structuring experiments. Carlo Altucci, E.Allahyari and Salvatore Amoruso: helped in Laser Surface Structuring experiments. Rosalba Fittipaldi and Antonio Vecchione: performed SEM measurements. Marcella Salvatore and Stefano Luigi Oscurato: carried out AFM and Raman measurements. Sergio Calatroni and Marcel Himmerlich: prepared the PC samples, carried out the XPS analysis and performed the SEY measurements. Martino Rimoldi: performed SEY analyses and sample conditioning measurements. Jijil JJ Nivas and Andrea Passarelli: integrated all the data and prepared the preliminary manuscript. All authors discussed the results and gave their feedback for the manuscript.

Declaration of Competing Interest

The authors declare no competing interests.

Acknowledgments

References

[1] O. Domínguez, K. Li, G. Arduini, E. Métral, G. Rumolo, F. Zimmermann, H. M. Cuna, First electron-cloud studies at the Large Hadron Collider, Phys. Rev. Spec. Top. - Accel. Beams. 16 (2013), https://doi.org/10.1103/PhysRevSTAB.16.011003.

[2] R. Cimino, T. Demma, Electron cloud in accelerators, Int. J. Mod. Phys. A. 29 (2014), 10.1142/S0217751×14300233.

[3] F. Zimmermann, Review of single bunch instabilities driven by an electron cloud, Phys. Rev. Spec. Top. - Accel. Beams. 7 (2004) 121–156, https://doi.org/10.1103/PhysRevSTAB.7.124801.

[4] G. Rumolo, F. Ruggiero, F. Zimmermann, Simulation of the electron-cloud build up and its consequences on heat load, beam stability, and diagnostics, Phys. Rev. Spec. Top. - Accel. Beams. 4 (2001), https://doi.org/10.1103/PhysRevSTAB.4.012801.

[5] M.A. Furman, M.T.F. Pivi, Probabilistic model for the simulation of secondary electron emission, Phys. Rev. Spec. Top. - Accel. Beams. 5 (2002) 82–99, https://doi.org/10.1103/PhysRevSTAB.5.124404.

[6] N. Balcon, D. Payan, M. Belhaj, T. Tondu, V. Inguimbert, Secondary electron emission on space materials: evaluation of the total secondary electron yield from surface potential measurements, in: IEEE Trans. Plasma Sci. (2012) https://doi.org/10.1109/TPS.2011.2172636.

[7] J.P. Boeuf, Tutorial: physics and modeling of Hall thrusters, J. Appl. Phys. (2017), https://doi.org/10.1063/1.4972269.

[8] V.E. Semenov, E. Rakova, R. Udiljak, D. Anderson, M. Lisak, J. Puech, Conformal mapping analysis of multipactor breakdown in waveguide irises, Phys. Plasmas. (2008), https://doi.org/10.1063/1.2884712.

[9] M. Ye, D. Wang, Y. He, Mechanism of total electron emission yield reduction using a micro-porous surface, J. Appl. Phys. (2017), https://doi.org/10.1063/1.4978760.

[10] J. Pierron, C. Inguimbert, M. Belhaj, J. Puech, M. Raine, Effect of rectangular grooves and checkerboard patterns on the electron emission yield, J. Appl. Phys. (2018), https://doi.org/10.1063/1.5028216.

[11] M. Pivi, F.K. King, R.E. Kirby, T.O. Raubenheimer, G. Stupakov, F.Le Pimpec, Sharp reduction of the secondary electron emission yield from grooved surfaces, J. Appl. Phys. (2008), https://doi.org/10.1063/1.3021149.

[12] M. Nishiwaki, S. Kato, Influence of electron irradiation and heating on secondary electron yields from non-evaporable getter films observed with in situ x-ray photoelectron spectroscopy, J. Vac. Sci. Technol. A Vacuum, Surfaces, Film. (2007), https://doi.org/10.1116/1.2738491.

[13] P.C. Pinto, S. Calatroni, H. Neupert, D. Letant-Delrieux, P. Edwards, P. Chiggiato, M. Taborelli, W. Vollenberg, C. Yin-Vallgren, J.L. Colaux, S. Lucas, Carbon coatings with low secondary electron yield, Vacuum (2013), https://doi.org/10.1016/j.vacuum.2013.03.001.

[14] I. Montero, L. Olano, L. Aguilera, M.E. Dávila, U. Wochner, D. Raboso, P. Martín-Iglesias, Low-secondary electron emission yield under electron bombardment of microstructured surfaces, looking for multipactor effect suppression, J. Electron. Spectros. Relat. Phenomena. (2020), https://doi.org/10.1016/j.elspec.2019.02.001.

[15] L. Aguilera, I. Montero, M.E. Dávila, A. Ruiz, L. Galán, V. Nistor, D. Raboso, J. Palomares, F. Soria, CuO nanowires for inhibiting secondary electron emission, J. Phys. D. Appl. Phys. (2013), https://doi.org/10.1088/0022-3727/46/16/165104.

[16] C. Swanson, I.D. Kaganovich, Modeling of reduced secondary electron emission yield from a foam or fuzz surface, J. Appl. Phys. (2018), https://doi.org/10.1063/1.5008261.

[17] M. Ye, Y.N. He, S.G. Hu, R. Wang, T.C. Hu, J. Yang, W.Z. Cui, Suppression of secondary electron yield by micro-porous array structure, J. Appl. Phys. (2013), https://doi.org/10.1063/1.4792514.

[18] J.M. Sattler, R.A. Coutu, R. Lake, T. Laurvick, T. Back, S. Fairchild, Modeling micro-porous surfaces for secondary electron emission control to suppress multipactor, J. Appl. Phys. (2017), https://doi.org/10.1063/1.4997465.

[19] R. Valizadeh, O.B. Malyshev, S. Wang, S.A. Zolotovskaya, W.A. Gillespie, A. Abdolvand, Low secondary electron yield engineered surface for electron cloud mitigation, Appl. Phys. Lett. (2014), https://doi.org/10.1063/1.4902993.

[20] S. Calatroni, E. Garcia-Tabares Valdivieso, H. Neupert, V. Nistor, A.T. Perez Fontenla, M. Taborelli, P. Chiggiato, O. Malyshev, R. Valizadeh, S. Wackerow, S. A. Zolotovskaya, W.A. Gillespie, A. Abdolvand, First accelerator test of vacuum components with laser-engineered surfaces for electron-cloud mitigation, Phys. Rev. Accel. Beams. (2017), https://doi.org/10.1103/PhysRevAccelBeams.20.113201.

[21] S. Calatroni, E. Garcia-Tabares Valdivieso, A.T. Perez Fontenla, M. Taborelli, H. Neupert, M. Himmerlich, P. Chiggiato, D. Bajek, S. Wackerow, A. Abdolvand, Optimization of the secondary electron yield of laser-structured copper surfaces at room and cryogenic temperature, Phys. Rev. Accel. Beams. (2020), https://doi.org/10.1103/PhysRevAccelBeams.23.033101.

[22] R. Valizadeh, O.B. Malyshev, S. Wang, T. Sian, M.D. Cropper, N. Sykes, Reduction of secondary electron yield for E-cloud mitigation by laser ablation surface engineering, Appl. Surf. Sci. (2017), https://doi.org/10.1016/j.apsusc.2017.02.013.

[23] R. Valizadeh, O.B. Malyshev, T. Sian, J.S. Colligon, Q. Li, W. Perrie, T. Photon, M. Manchester, Laser ablated surface engineering : from discovery to machine application, ECLOUD'18 Proc. (2020) 209–216, https://doi.org/10.23732/CYRCP-2020-007.209.

[24] E. Stratakis, J. Bonse, J. Heitz, J. Siegel, G.D. Tsibidis, E. Skoulas, A. Papadopoulos, A. Mimidis, A.C. Joel, P. Comanns, J. Krüger, C. Florian, Y. Fuentes-Edfuf, J. Solis, W. Baumgartner, Laser engineering of biomimetic surfaces, Mater. Sci. Eng. R Reports. (2020), https://doi.org/10.1016/j.mser.2020.100562.

[25] J. Bonse, S. Hohm, S.V. Kirner, A. Rosenfeld, J. Kruger, Laser-induced periodic surface structures-a scientific evergreen, IEEE J. Sel. Top. Quantum Electron. (2017), https://doi.org/10.1109/JSTQE.2016.2614183.

[26] R. Buividas, M. Mikutis, S. Juodkazis, Surface and bulk structuring of materials by ripples with long and short laser pulses: recent advances, Prog. Quantum Electron. (2014), https://doi.org/10.1016/j.pquantelec.2014.03.002.

[27] A.Y. Vorobyev, C. Guo, Direct femtosecond laser surface nano/microstructuring and its applications, Laser Photonics Rev 7 (2013) 385–407, https://doi.org/10.1002/lpor.201200017.

[28] G. Rumolo, H. Bartosik, E. Belli, P. Dijkstal, G. Iadarola, K. Li, L. Mether, A. Romano, M. Schenk, F. Zimmermann, Electron cloud effects at the LHC and LHC injectors, in: IPAC 2017 Eighth Int. Part. Accel. Conf. (2017) 30–36 http://jacow.org/ipac2017/doi/JACoW-IPAC2017-MOZA1.html.

[29] B. Lindstrom, A. Apollonio, P. Bélanger, M. Dziadosz, A. Gorzawski, L. Grob, E. B. Holzer, A. Lechner, R. Schmidt, M. Valette, D. Valuch, D. Wollmann, Results of UFO dynamics studies with beam in the LHC, J. Phys. Conf. Ser. (2018), https://doi.org/10.1088/1742-6596/1067/2/022001.

[30] L. Grob, A. Apollonio, C. Charvet, E.G.-T. Valdivieso, Dust analysis from LHC vacuum system to identify the source of macro particle-beam-interactions, in: 10th Int. Part. Accel. Conf. (IPAC2019, Melbourne, JACoW Publishing, 2019, pp. 1082–1085, https://doi.org/10.18429/JACoW-IPAC2019-MOPTS094.

[31] S. Gräf, F.A. Müller, Polarisation-dependent generation of fs-laser induced periodic surface structures, Appl. Surf. Sci. 331 (2015) 150–155, https://doi.org/10.1016/j.apsusc.2015.01.056.

[32] H. Zhang, J.P. Colombier, S. Witte, Laser-induced periodic surface structures: arbitrary angles of incidence and polarization states, Phys. Rev. B. 101 (2020), 245430, https://doi.org/10.1103/PhysRevB.101.245430.

[33] L. Ferreira and M. Malabaila, Cleaning procedure for copper parts, Cern EDMS Doc. 1084640. (2014). https://edms.cern.ch/document/1084640/1.

[34] J.M. Liu, Simple technique for measurements of pulsed Gaussian-beam spot sizes, Opt. Lett. 7 (1982) 196, https://doi.org/10.1364/OL.7.000196.

[35] P. Gecys, E. Markauskas, M. Gedvilas, G. Raciukaitis, I. Repins, C. Beall, Ultrashort pulsed laser induced material lift-off processing of CZTSe thin-film solar cells, Sol. Energy. 102 (2014) 82–90, https://doi.org/10.1016/J.SOLENER.2014.01.013.

[36] J. Krüger, W. Kautek, Ultrashort pulse laser interaction with dielectrics and polymers, in: T. Lippert (Ed.), Polym. Light Adv. Polym. Sci. 168, Springer, Berlin, Heidelberg, 2004: pp. 247–290. https://doi.org/10.1007/b12683.

[37] D. Bouilly, D. Perez, L.J. Lewis, Damage in materials following ablation by ultrashort laser pulses: a molecular-dynamics study, Phys. Rev. B - Condens. Matter Mater. Phys. 76 (2007), 184119, https://doi.org/10.1103/PhysRevB.76.184119.

[38] M.S. Sidhu, P. Munjal, K.P. Singh, High-fidelity large area nano-patterning of silicon with femtosecond light sheet, Appl. Phys. A. 124 (2018) 46, https://doi.org/10.1007/s00339-017-1459-3.

[39] M. Gedvilas, J. Mikšys, G. Račiukaitis, Flexible periodical micro- and nano-structuring of a stainless steel surface using dual-wavelength double-pulse picosecond laser irradiation, RSC Adv 5 (2015) 75075–75080, https://doi.org/10.1039/C5RA14210E.

[40] C.A. Zuhlke, G.D. Tsibidis, T. Anderson, E. Stratakis, G. Gogos, D.R. Alexander, Investigation of femtosecond laser induced ripple formation on copper for varying incident angle, AIP Adv 8 (2018), https://doi.org/10.1063/1.5020029.

[41] M. Malinauskas, A. Žukauskas, S. Hasegawa, Y. Hayasaki, V. Mizeikis, R. Buividas, S. Juodkazis, Ultrafast laser processing of materials: from science to industry, Light Sci. Appl. 5 (2016) e16133, https://doi.org/10.1038/lsa.2016.133.

[42] I. Gnilitskyi, V. Gruzdev, N.M. Bulgakova, T. Mocek, L. Orazi, Mechanisms of high-regularity periodic structuring of silicon surface by sub-MHz repetition rate ultrashort laser pulses, Appl. Phys. Lett. 109 (2016), 143101, https://doi.org/10.1063/1.4963784.

[43] R.Le Harzic, D. Dörr, D. Sauer, M. Neumeier, M. Epple, H. Zimmermann, F. Stracke, Large-area, uniform, high-spatial-frequency ripples generated on silicon using a nanojoule-femtosecond laser at high repetition rate, Opt. Lett. 36 (2011) 229, https://doi.org/10.1364/ol.36.000229.

[44] J. Bonse, S. Gräf, Maxwell meets marangoni—a review of theories on laser-induced periodic surface structures, Laser Photon. Rev. 14 (2020), 2000215, https://doi.org/10.1002/lpor.202000215.

[45] M. Huang, F. Zhao, Y. Cheng, N. Xu, Z. Xu, Origin of laser-induced near-subwavelength ripples: interference between surface plasmons and incident laser, ACS Nano 3 (2009) 4062–4070, https://doi.org/10.1021/nn900654v.

[46] V. Petit, M. Taborelli, H. Neupert, P. Chiggiato, M. Belhaj, Role of the different chemical components in the conditioning process of air exposed copper surfaces, Phys. Rev. Accel. Beams. 22 (2019), https://doi.org/10.1103/PhysRevAccelBeams.22.083101.

[47] G.D. Tsibidis, A. Mimidis, E. Skoulas, S.V. Kirner, J. Krüger, J. Bonse, E. Stratakis, Modelling periodic structure formation on 100Cr6 steel after irradiation with femtosecond-pulsed laser beams, Appl. Phys. A. 124 (2018) 27, https://doi.org/10.1007/s00339-017-1443-y.

[48] S. He, J.J. Nivas, K.K. Anoop, A. Vecchione, M. Hu, R. Bruzzese, S. Amoruso, Surface structures induced by ultrashort laser pulses: formation mechanisms of ripples and grooves, Appl. Surf. Sci. 353 (2015), https://doi.org/10.1016/j.apsusc.2015.07.016.

[49] S. Sarbada, Y.C. Shin, Superhydrophobic contoured surfaces created on metal and polymer using a femtosecond laser, Appl. Surf. Sci. 405 (2017) 465–475, https://doi.org/10.1016/J.APSUSC.2017.02.019.

[50] S. Maragkaki, A. Elkalash, E.L. Gurevich, Orientation of ripples induced by ultrafast laser pulses on copper in different liquids, Appl. Phys. A. 123 (2017) 721, https://doi.org/10.1007/s00339-017-1336-0.

[51] J. Bonse, J. Krüger, Pulse number dependence of laser-induced periodic surface structures for femtosecond laser irradiation of silicon, J. Appl. Phys. 108 (2010), 034903, https://doi.org/10.1063/1.3456501.

[52] D. Bajek, S. Wackerow, D.A. Zanin, L. Baudin, K. Bogdanowicz, E.G.T. Valdivieso, S. Calatroni, B. Di Girolamo, M. Sitko, M. Himmerlich, M. Taborelli, P. Chiggiato, A. Abdolvand, Role of surface microgeometries on electron escape probability and secondary electron yield of metal surfaces, Sci. Rep. (2020), https://doi.org/10.1038/s41598-019-57160-w.

[53] N. Destouches, N. Crespo-Monteiro, G. Vitrant, Y. Lefkir, S. Reynaud, T. Epicier, Y. Liu, F. Vocanson, F. Pigeon, Self-organized growth of metallic nanoparticles in a thin film under homogeneous and continuous-wave light excitation, J. Mater. Chem. C. 2 (2014) 6256–6263, https://doi.org/10.1039/c4tc00971a.

[54] A. Talbi, A. Petit, A. Melhem, A. Stolz, C. Boulmer-Leborgne, G. Gautier, T. Defforge, N. Semmar, Nanoparticles based laser-induced surface structures formation on mesoporous silicon by picosecond laser beam interaction, Appl. Surf. Sci. 374 (2016) 31–35, https://doi.org/10.1016/j.apsusc.2015.09.003.

[55] K.R.P. Kafka, D.R. Austin, H. Li, A.Y. Yi, J. Cheng, E.A. Chowdhury, Time-resolved measurement of single pulse femtosecond laser-induced periodic surface structure formation induced by a pre-fabricated surface groove, Opt. Express. 23 (2015) 19432, https://doi.org/10.1364/oe.23.019432.

[56] M. Guillermin, F. Garrelie, N. Sanner, E. Audouard, H. Soder, Single- and multi-pulse formation of surface structures under static femtosecond irradiation, Appl. Surf. Sci. 253 (2007) 8075–8079, https://doi.org/10.1016/j.apsusc.2007.02.093.

[57] L. Debbichi, M.C. Marco De Lucas, J.F. Pierson, P. Krüger, Vibrational properties of CuO and Cu 4O 3 from first-principles calculations, and raman and infrared spectroscopy, J. Phys. Chem. C. 116 (2012) 10232–10237, https://doi.org/10.1021/jp303096m.

[58] V.S. Levitskii, V.I. Shapovalov, A.E. Komlev, A.V. Zav'yalov, V.V. Vit`ko, A. A. Komlev, E.S. Shutova, Raman spectroscopy of copper oxide films deposited by reactive magnetron sputtering, Tech. Phys. Lett. 41 (2015) 1094–1096, https://doi.org/10.1134/S106378501511022X.

[59] J. Ghijsen, L.H. Tjeng, J. Van Elp, H. Eskes, J. Westerink, G.A. Sawatzky, M. T. Czyzyk, Electronic structure of Cu2O and CuO, Phys. Rev. B. 38 (1988) 11322–11330, https://doi.org/10.1103/PhysRevB.38.11322.

[60] M.C. Biesinger, B.P. Payne, A.P. Grosvenor, L.W.M. Lau, A.R. Gerson, R.S.C. Smart, Resolving surface chemical states in XPS analysis of first row transition metals,

oxides and hydroxides: Cr, Mn, Fe, Co and Ni, Appl. Surf. Sci. 257 (2011) 2717–2730, https://doi.org/10.1016/j.apsusc.2010.10.051.

[61] H. Panuganti, E. Chevallay, V. Fedosseev, M. Himmerlich, Synthesis, surface chemical analysis, lifetime studies and degradation mechanisms of Cs-K-Sb photocathodes, Nucl. Instruments Methods Phys. Res. Sect. A Accel. Spectrometers, Detect. Assoc. Equip. 986 (2021), 164724, https://doi.org/10.1016/j.nima.2020.164724.

[62] M.P. Seah, The quantitative analysis of surfaces by XPS: a review, Surf. Interface Anal. 2 (1980) 222–239, https://doi.org/10.1002/sia.740020607.

[63] R. Cimino, M. Commisso, D.R. Grosso, T. Demma, V. Baglin, R. Flammini, R. Larciprete, Nature of the decrease of the secondary-electron yield by electron bombardment and its energy dependence, Phys. Rev. Lett. (2012), https://doi.org/10.1103/PhysRevLett.109.064801.

[64] G. Iadarola, H. Bartosik, K. Li, L. Mether, A. Romano, G. Rumolo, M. Schenk, Performance limitations from electron cloud in 2015, in: 6th Evian Work, LHC Beam Oper. (2015) 101–110. https://cds.cern.ch/record/2294523.